20 August 1999

Analysis of the X-Ray Tomograph Data of the BOS MDT Prototype Chamber

H. Kroha, A. Manz and A. Ostapchuk
Max-Planck-Institut für Physik, Munich

Abstract

The complete X-ray tomograph data of the BOS MDT prototype chamber for the ATLAS muon spectrometer have been analyzed. The geometrical parameters of the chamber determined from the average of all X-ray scans are in good agreement with the design values. The spread of the measured wire positions with respect to the fitted wire grid is 17.0 μm (19.0 μm) RMS in the z coordinate and 18.2 μm (19.3 μm) RMS in y on the readout (high voltage) side. The errors include the average measuring uncertainty of the X-ray tomograph estimated to be 4 μm RMS in z and 6 μm RMS in y from the reproducibility of repeated measurements in the same chamber position.

Contents

1 Introduction

The complete X-ray tomograph [1] data of the full-scale prototype of a BOS MDT chamber constructed in February 1998 at MPI Munich [2] have been analyzed. The chamber has a tube length of 3800 mm and a width of 2160 mm, the largest chamber width in the barrel part of the ATLAS muon spectrometer. It contains 432 drift tubes, 72 in each of the 6 tube layers. The chamber has been constructed according to the procedures described in the Technical Design Report for the ATLAS muon spectrometer [3].

21 X-ray scans of the chamber have been performed at CERN. After analysis of the X-ray shadowgrams, the wire-coordinate data for 9 scans of the HV side of the chamber, 3 scans of the RO side and 3 scans of the middle part of the chamber have been made available for analysis on the X-ray tomograph web page.

The 9 scans of the HV side were performed in 4 different chamber orientations (see Figure 1):

- two scans (numbers 7 and 8 in the sequential scan numbering) in the initial orientation ("r1") ,
- two scans (9 and 11) after rotation of the chamber by 180^o around the x-axis (orientation "r2"),
- two scans (12 and 14) after rotation of the chamber by 180^o around the y-axis with respect to orientation r2 (orientation "r3"),
- and three scans (15, 20 and 21) after rotation of the chamber by 180^o around the x-axis with respect to orientation r3 (orientation "r4").

The three scans of the RO side are the following:

- one scan (10) in orientation r2,
- one scan (13) in orientation r3 and
- one scan (17) in orientation r4.

Out of the 432 wires of the chamber, 320–330 were reconstructed for the different scans. Measurement of the remaining wires was obscured by the long beams. No wire coordinates provided by the X-ray tomograph have been discarded in the analysis.

Analysis of the X-ray measurements allows to determine the geometrical parameters of the prototype chamber as well as the intrinsic resolution of the X-ray tomograph. Comparison of the wire coordinates measured by the X-ray tomograph with the measurements of wire positions in individual tubes before assembly of the chamber [2] gives information about the contributions of drift tube and chamber assembly to the mechanical accuracy of the chamber.

2 Comparison with the Ideal Wire Grid

The geometrical parameters of the chamber are determined by the assembly jigging, the combs and sphere towers, which are set up on a flat granite table and have been measured using 3D metrology (see [2]). Accordingly, the design parameters of the prototype chamber at 20° C are:
y- and z-pitch on high voltage (HV) and readout (RO) side:

$$\begin{aligned} y\mathrm{-pitch} &= (26054 \pm 10)\ \mu\mathrm{m}, \\ z\mathrm{-pitch} &= (30036 \pm 0.6)\ \mu\mathrm{m}; \end{aligned}$$

z-shift and y-separation (defined between the nearest wire planes) between the two multilayers (ML):

$$\begin{aligned} \Delta_y^{HV} &= (347.040 \pm 0.010)\ \mathrm{mm}\ \ (\mathrm{HV\ side}), \\ \Delta_y^{RO} &= (347.072 \pm 0.010)\ \mathrm{mm}\ \ (\mathrm{RO\ side}), \\ \Delta_z^{HV} &= 0\ \mathrm{mm}\ \ (\mathrm{HV\ side}), \\ \Delta_z^{RO} &= 0\ \mathrm{mm}\ \ (\mathrm{RO\ side}). \end{aligned}$$

The vertical y-pitch was intentionally increased by (40 ± 10) μm compared to the nominal value of 26.011 mm for the construction of the prototype chamber to avoid touching of tube layers during glueing. On the readout side, the y-separation between multilayers is increased by a common offset of 32 μm of the wire positions in all drift tubes of the second multilayer known precisely from the X-ray measurements of wire positions in individual tubes (see [2]).

For the wide BOS chambers, correct compensation of the gravitational sag of the cross plates during glueing of each tube layer is an essential part of the assembly process. The sag of the outer cross plates of the prototype chamber was controlled with the force compensation system and optical cross plate sag monitors to be below 10 μm for each tube layer glued (see [2]).

The wire positions measured in the X-ray scans were fitted with an ideal grid with the expected geometrical parameters of the chamber. The y- and z-coordinate of the origin of the grid and the angular orientation of the grid around the x-axis with respect to the X-ray tomograph coordinate system are not relevant for the chamber accuracy and were treated as three free parameters in the fit.

The mechanical accuracy of the chamber can be characterised by the RMS widths of the residual distributions of the measured wire positions in y and z with respect to their nominal values. The results of the fit for the whole chamber and for each multilayer separately are shown in Table 1 for the scans on the high-voltage (HV) and on readout (RO) side and their averages.

The average RMS values are close to the specified 20 μm [3], but their variations from scan to scan are large. The value of $RMS_{\delta y}^{tot}$ varies from 19.4 μm up to 26.4 μm for the 9 scans of the HV side. This wide range of variation is not compatible with the expected X-ray tomograph resolution. Possible reasons for the large variations of the X-ray tomograph results have been investigated.

Table 1: RMS widths [μm] of the distributions of the residuals δy and δz of the wire coordinates from the X-ray measurements with respect to the expected ideal grid with the fixed geometrical parameters: y-pitch = 26.054 mm, z-pitch = 30.036 mm, Δ_y^{HV} = 347.040 mm, Δ_y^{RO} = 347.072 mm, $\Delta_z^{HV} = 0$, $\Delta_z^{RO} = 0$, sag of chamber ends = 0. The RMS values are also given separately for the two multilayers ML1 and ML2 numbered in the assembly sequence.

Scan	RMS_y^{tot}	RMS_z^{tot}	RMS_y^{ML1}	RMS_z^{ML1}	RMS_y^{ML2}	RMS_z^{ML2}
HV-r1-07	26.4	22.6	28.8	17.8	23.9	22.5
HV-r1-08	24.5	20.6	25.0	17.2	23.7	22.4
HV-r2-09	20.4	19.5	22.4	15.6	18.2	22.2
HV-r2-11	19.4	19.8	20.7	14.2	18.0	22.2
HV-r3-12	26.0	20.1	22.4	16.4	20.6	22.5
HV-r3-14	21.7	21.0	22.3	16.6	20.8	23.4
HV-r4-15	23.4	20.2	23.4	16.4	22.3	20.9
HV-r4-20	22.5	20.3	22.5	16.2	21.7	20.6
HV-r4-21	22.1	19.6	22.4	16.3	21.3	20.3
Average HV-side	23.0 ±2.1	20.4 ±1.1	23.3 ±2.1	16.3 ±0.9	21.2 ±2.0	21.9 ±2.4
RO-r2-10	18.6	17.7	15.1	12.4	21.7	20.5
RO-r3-13	22.9	20.0	16.5	13.6	19.1	21.8
RO-r4-17	22.6	21.4	16.0	15.2	20.1	22.7
Average RO-side	21.4 ±1.6	19.7 ±1.5	15.9 ±0.6	13.7 ±1.1	20.3 ±1.1	21.7 ±0.9

3 Chamber Deformations During X-Ray Measurements

Both from the readings of the RASNIK cross plate sag monitors (see [2]) and from the X-ray tomograph data, *global* deformations of the high voltage and readout ends of the chamber were found which exceed the expectations from the Bessel support of the cross plates and which vary for the different orientations of the chamber in the tomograph (see Figures 2 and 3). The deformations observed can be described by a parabola. One concludes that the chamber in its different orientations was not supported free of external moments in the tomograph as required.

For the evaluation of the accuracy of the chamber, the global deformations of the chamber ends in the tomograph setup have to be taken into account.

The fits of the measured wire coordinates with a grid were repeated with the same geometrical parameters as used for Table 1 but with a common parabolic sag of both multilayers as additional free parameter. As expected, the RMS_y values improve (see Table 2).

As expected from the data in Figures 2 and 3, the largest fitted sag of approximately 50 μm was found on the HV-side in orientation r1. Consequently, the most significant improvement of the RMS value of the y-residuals occurs for scans 7 and 8. Still the variations of the $RMS_{\delta y}$ values for the different scans are larger than expected: from 18.5 μm to 24.2 μm on the HV side and from 17.7 μm to 22.3 μm on the RO side.

Table 2: RMS widths [μm] of the distributions of the residuals δy and δz of the wire coordinates from the X-ray measurements with respect to the expected ideal grid with the fixed geometrical parameters: y-pitch $= 26.054$ mm, z-pitch $= 30.036$ mm, $\Delta_y^{HV} = 347.040$ mm, $\Delta_y^{RO} = 347.072$ mm, $\Delta_z^{HV} = 0$, $\Delta_z^{RO} = 0$, and the parabolic sag of the chamber ends as free parameter. The RMS values are also given separately for the two multilayers ML1 and ML2 numbered in the assembly sequence.

Scan	Sag [μm]	$RMS_y^{\rm tot}$	$RMS_z^{\rm tot}$	RMS_y^{ML1}	RMS_z^{ML1}	RMS_y^{ML2}	RMS_z^{ML2}
HV-r1-07	-53	19.2	22.8	21.4	17.8	16.6	22.6
HV-r1-08	-49	19.2	20.5	19.6	17.2	17.3	22.4
HV-r2-09	-23	19.4	19.5	20.2	14.3	17.1	22.2
HV-r2-11	-18	18.5	19.8	20.8	15.6	16.7	22.2
HV-r3-12	28	24.2	20.1	20.4	16.4	18.5	22.5
HV-r3-14	24	20.1	21.0	20.4	16.6	19.4	23.4
HV-r4-15	29	21.3	20.2	21.2	16.4	20.3	20.9
HV-r4-20	28	20.2	20.2	20.0	16.2	19.6	20.6
HV-r4-21	26	20.3	19.6	20.3	16.3	19.6	20.3
Average HV-side		20.3 $\pm$1.6	20.4 $\pm$1.1	20.5 $\pm$0.4	16.3 $\pm$1.1	18.3 $\pm$1.9	21.9 $\pm$1.0
RO-r2-10	17	17.7	17.7	21.0	20.5	14.0	12.4
RO-r3-13	-1	22.9	20.0	19.1	21.7	16.3	13.6
RO-r4-17	-7	22.3	21.6	19.7	22.7	15.7	15.2
Average RO-side		21.0 $\pm$2.3	19.8 $\pm$1.5	19.9 $\pm$1.4	21.6 $\pm$1.5	15.3 $\pm$1.0	13.7 $\pm$1.5

4 Reproducibility of the X-Ray Tomograph Measurements

In order to understand the variations in the results of the X-ray tomograph scans, the reproducibility of the measurements from repeated scans of the chamber in the same position has been evaluated. The differences between two subsequent measurements i and j in the same position, i.e. the mean and RMS of the distributions of the differences

$$\begin{aligned} \Delta y &= \delta y_i - \delta y_j \quad \text{and} \\ \Delta z &= \delta z_i - \delta z_j \end{aligned}$$

of the residuals δy and δz of the wire coordinates with respect to the expected grid with sag (see previous section), are given in Table 3.

The RMS widths of the differences of the residuals of the wire coordinates vary considerably for the different chamber orientations in the tomograph. The average RMS widths are 4 μm for the z-coordinate and 7 μm for the y-coordinate in the multilayer which was on top during the scan. The reproducibility for the bottom multilayer is 1.5 times worse, 6 μm in z and 10 μm in y, respectively, which can be explained by the larger multiple scattering of the X-rays. The ratio of the widths for the z- and for the y-coordinate is about 0.6 for both multilayers which is

Table 3: Reproducibility of the X-ray tomograph measurements: mean and RMS [μm] of the differences Δy and Δz of the residuals of the measured wire coordinates with respect to the expected grid with sag for two subsequent scans of the chamber on the high voltage side in the same position (top and bottom multilayer separately and combined)

Scans	$< \Delta y >^{\rm tot}$	$RMS^{\rm tot}_{\Delta y}$	$< \Delta y >^{\rm top}$	$RMS^{\rm top}_{\Delta y}$	$< \Delta y >^{\rm bot}$	$RMS^{\rm bot}_{\Delta y}$
7– 8	−1.6	11.4	5.2	7.6	−10.4	9.4
9–11	−1.3	9.0	2.7	6.6	− 6.6	9.1
12–14	2.0	14.3	11.0	6.8	−11.4	10.5
15–20	-0.4	9.7	0.1	6.5	− 0.9	12.1
15–21	-0.5	11.4	7.2	7.1	− 8.6	9.2
Average	−0.4	11.2	5.2	6.9	− 7.6	10.1
Scans	$< \Delta z >^{\rm tot}$	$RMS^{\rm tot}_{\Delta z}$	$< \Delta z >^{\rm top}$	$RMS^{\rm top}_{\Delta z}$	$< \Delta z >^{\rm bot}$	$RMS^{\rm bot}_{\Delta z}$
7– 8	−0.7	7.3	−5.5	4.2	5.7	5.4
9–11	−1.4	5.0	−3.0	4.0	7.5	5.3
12–14	0.4	5.5	1.0	4.5	−0.3	6.4
15–20	−0.2	5.6	0.6	3.9	−1.2	6.8
15–21	0.3	5.1	0.1	4.2	0.5	5.8
Average	−0.3	5.7	−1.4	4.2	2.4	5.9

in agreement with the expected value of $\tan 30° = 0.58$ due to the 30° inclination of the X-ray beams with respect to the the y axis.

The total widths for the whole chamber, $RMS^{\rm tot}_{\Delta z} \simeq 6\mu$m and $RMS^{\rm tot}_{\Delta y} \simeq 11\mu$m, differ from the average of the values for top and bottom multilayers, obviously due to systematic shifts of the measured wire coordinates in the two multilayers from one scan to the other.

Information about the origin of the systematic effects can be obtained by studying the difference between repeated wire coordinate measurements as function of z, i.e. along the scan direction. The differences of the y- and z-residuals for the two subsequent scans no. 7 and 8 in the same position of the chamber,

$$\Delta y = \delta y_7 - \delta y_8 \ \text{ and } \ \Delta z = \delta z_7 - \delta z_8,$$

are shown as a function of z-coordinate of the wires in Figure 4 (for the top multilayer) and Figure 5 (for the bottom multilayer).

Significant systematic effects are visible: large fluctuations near the locations of the long beams which absorb and scatter the X-rays, average offsets from zero and slopes in scan direction. The effects are studied further by projecting the y- and z-coordinates of the wires in the directions perpendicular to and measured directly by the two X-ray beams:

$$\begin{aligned} \Delta_{\rm left} &= \cos(30°) \cdot \Delta z + \sin(30°) \cdot \Delta y, \\ \Delta_{\rm right} &= cos(30°) \cdot \Delta z - \sin(30°) \cdot \Delta y. \end{aligned}$$

The variables $\Delta_{\rm left}$ and $\Delta_{\rm right}$ describe the reproducibility of the wire position measurements with respect to the directions of the left and right X-ray beam in scan direction, respectively.

The z-dependence of the new variables is shown in Figure 6 for the top multilayer and in Figure 7 for the bottom multilayer.

The analysis leads to the following conclusions on the systematics of the X-ray measurements:

1. Large fluctuations are observed in both coordinates in the regions close to the shadows of the long-beams which have not been corrected.
2. The wire coordinates measured by the right X-ray beam are relatively stable along the scan direction with average offsets of $\Delta_{\rm right}$ from zero of ~ -10 μm for the top multilayer and $\sim +10$ μm for the bottom multilayer. The offsets can be explained by a change of the right X-ray direction between the two scans.
3. The difference of the wire coordinates measured by the left X-ray beam show a systematic trend across the width of the chamber which can be explained by a drift of the direction of the left X-ray beam during one of the two scans.

Similar systematic effects were found in the comparison of the other repeated scans in the same position. They broaden the residual distributions of the measured wire coordinates and explain the large variations of RMS_y and RMS_z from scan to scan (see Table 2). In particular, they deteriorate the accuracy in the measurement of the multilayer separations in y and z. According to Table 3, the reproducibility of the measurement of the multilayer separations

$$< \Delta y >^{\rm top} - < \Delta y >^{\rm bot} \quad \text{and} \quad < \Delta z >^{\rm top} - < \Delta z >^{\rm bot}$$

varies in the range 1 to 22.4 μm for y and -11.2 to -0.4 μm for z.

To get rid of the systematic uncertanities in the X-ray measurement of the multilayer separations in y and z and the y- and z-pitches for the evaluation of the chamber accuracy, these parameters have to be left free in the grid fit. The remaining uncertainty in the wire coordinate measurements is the intrinsic resolution of the X-ray tomograph which can be estimated from the reproducibility of repeated scans by dividing the average $RMS_{\Delta y}$ and $RMS_{\Delta z}$ in Table 3 by $\sqrt{2}$ since both scans are affected by the measurement errors.

The y-resolution of the X-ray tomograph for the measurement of the BOS prototype chamber is therefore 5 μ for the top multilayer and 7 μm for the bottom multilayer. The z-resolution is 3 μm and 4 μm, respectively, for the top and the bottom multilayer. The average X-ray tomograph resolutions for the whole chamber are

$$\sigma_y^{\rm tomo} \simeq 6 \quad \mu\text{m and} \tag{1}$$

$$\sigma_z^{\rm tomo} \simeq 3.5\ \mu\text{m}. \tag{2}$$

5 Global Fit of the Wire Grid

Given the mechanical tolerances of the jigging [2], [3] (see Table 5) and the systematic uncertainties of the X-ray tomograph measurements, the geometrical parameters and the accuracy of the chamber are best evaluated by fitting a wire grid to the wire coordinates measured in

Table 4: Results from the global fit of a wire grid to the data from the X-ray tomograph scans on the high voltage (HV) and readout (RO) side and at intermediate x-positions (see Figure 1). Repeated scans for the same chamber orientation are grouped together. For the different scans, the average sagitta of all layers, y- and z-pitch and the separations Δ_y and Δ_z between multilayers are determined as parameters in the fit. The RMS widths and standard deviations (from fit of a Gaussian) of the residual distributions in y and z are also shown.

Scan	Sag $[\mu m]$	y-pitch $[mm]$	z-pitch $[mm]$	Δ_y $[mm]$	Δ_z $[\mu m]$	RMS_y^{tot} $[\mu m]$	RMS_z^{tot} $[\mu m]$	σ_y^{tot} $[\mu m]$	σ_z^{tot} $[\mu m]$
HV-r1-07	-53	26.057	30.0361	347.038	-22	18.6	20.5	18.5	18.7
HV-r1-08	-51	26.054	30.0362	347.028	-5	18.3	20.3	17.6	18.5
HV-r2-09	-23	26.058	30.0364	347.041	-6	18.4	18.6	15.9	16.6
HV-r2-11	-19	26.057	30.0362	347.036	-11	18.3	19.0	17.1	15.9
HV-r3-12	$+27$	26.059	30.0363	347.058	$+10$	19.0	19.4	16.8	18.1
HV-r3-14	$+23$	26.059	30.0362	347.062	$+13$	19.5	20.3	17.5	18.0
HV-r4-15	$+28$	26.058	30.0362	347.041	-17	20.3	18.8	18.8	16.3
HV-r4-20	$+28$	26.059	30.0361	347.039	-18	19.3	18.5	18.2	17.3
HV-r4-21	$+25$	26.058	30.0360	347.026	-15	19.7	18.4	18.0	16.4
Average HV-side		26.058 ± 0.0005	30.0362 ± 0.0001	347.041 ± 0.011	-8 ± 11	19.0 ± 0.8	19.3 ± 0.8	17.6 ± 0.9	17.3 ± 1.2
2-r4-19	$+25$	26.058	30.0361	347.045	-17	17.7	17.3	15.9	14.2
3-r4-16	$+4$	26.058	30.0361	347.050	-28	15.0	16.1	12.5	15.5
4-r4-18	-4	26.060	30.0359	347.081	-20	15.5	16.7	13.7	16.4
RO-r2-10	$+16$	26.058	30.0362	347.061	$+12$	17.3	16.6	15.0	14.0
RO-r3-13	-14	26.061	30.0362	347.086	$+17$	16.7	18.3	14.8	16.4
RO-r4-17	-8	26.060	30.0361	347.087	-20	17.0	19.7	14.6	17.2
Average RO-side		26.060 ± 0.0013	30.0362 ± 0.00005	347.078 ± 0.012	$+3$ ± 16	17.0 ± 0.2	18.2 ± 1.3	14.8 ± 0.2	15.9 ± 0.9

each scan with the y- and z-pitch, the y- and z-separation between multilayers and the common sagitta of all layers in y-direction as free parameters. The results for the different scans and their average are given in Table 4. Included are the rms widths of the residual distributions and their standard deviations (from fit of a Gaussian) which can be used to evaluate the overall accuracy of the chamber assembly. The wire coordinate errors contain a non-negligible contribution from the resolution of the X-ray tomograph (see previous section). The residual distributions for two typical scans are shown in Figures 8 and 9.

The design values for the y- and z-pitch and the y- and z-separations between the multilayers (see [2]) from measurement of the assembly jigging, are well reproduced by the averaged X-ray tomograph results within the measurement errors (see Table 5). The measured y- and z-separations between multilayers vary considerably from scan to scan indicating the intrinsic systematic errors of the X-ray measurements. The small variations in the average z-pitch from scan to scan may have been caused by temperature variations of the chamber in the X-ray tomograph.

Table 5: Comparison of the average X-ray tomograph measurements of the geometrical chamber parameters with the design values (at 20°C) and average RMS values of the measured wire coordinates (including the resolution of the X-ray tomograph measurements)

	HV side		RO side	
	X-ray	Design value	X-ray	Design value
y-pitch [μm]	26058 ± 0.5	26054 ± 10	26060 ± 1.3	26054 ± 10
z-pitch [μm]	30036.2 ± 0.1	30036.8 ± 0.6	30036.2 ± 0.05	30036.8 ± 0.6
y-sep. ML [mm]	347.041 ± 0.011	347.040 ± 0.010	347.078 ± 0.012	347.072 ± 0.010
z-sep. ML [μm]	-8 ± 11	0 ± 10	3 ± 16	0 ± 10
RMS_y [μm]	19.0 ± 0.8		17.0 ± 0.2	
RMS_z [μm]	19.3 ± 0.8		18.2 ± 1.3	

6 Uniformity of Tube Layers

For each individual tube layer the y-residuals of the wires with respect to the gobal fit were fitted with a parabola

$$\delta y(z) = a_y + b_y \cdot z + c_y \cdot z^2$$

and the z-residuals with a a straight line

$$\delta z(z) = a_z + b_z \cdot z.$$

The average values of the parameters a_y, b_y, c_y, a_z and b_z for all scans as well as the average shifts $< \delta y >$ and $< \delta z >= a_z$ and the spreads $RMS_{\delta y}$ and $RMS_{\delta z}$ with respect to the fitted grid are shown for each tube layer in Table 6. The parameters are given in the chamber coordinate frame for the initial orientation r1 (see Figure 1) with the y-axis pointing upwards and the z-axis in scan direction. They allow to evaluate the uniformity of the chamber parameters for all layers.

With the chamber width $W = 2160$ mm, the sagitta of the tube layers after subtraction of the common sag on the supports in the X-ray tomograph is $c_y \cdot (W/2)^2$. Beyond the common sag, there are no deformations of individual tube layers significantly above the specification for the cross plate sag compensation.

Tables 7 and 8 show the averaged measured geometrical parameters of individual tube layers, z-pitch, z-shift and average y-separation. The z-pitch of a layer is given by $\delta z_0[\mu\mathrm{m}] + b_z \cdot \delta z_0[\mathrm{m}]$ where δz_0 is the average global z-pitch of the chamber. The uniformity of the chamber parameters is very good with respect to the tolerances of the assembly tooling which fulfill the specifications.

The only significant deviations from the design parameters of the chamber are global z-shifts of $+16$ μm and -19 μm of the two outer tube layers with respect to the fitted grid, in the first multilayer on the HV side and in the second multilayer on the RO side. The same sphere tower interface is responsible for z-positioning in both cases and the two shifts point in the same direction in the coordinate frame of the assembly jigging. The z-shifts are the reason for the larger RMS values for the z- compared to the y-coordinate. The foreseen optical sphere monitors allow to detect such shifts if they should occur during series production.

Table 6: Geometrical parameters of individual tube layers (average of all scans). The layers are numbered in the assembly sequence, from the inside out for each multilayer (ML 1: layers 1–3, ML 2: layers 4–5).

Layer	a_y $[\mu m]$	b_y $[\mu m/m]$	c_y $[\mu m/m^2]$	$< \delta y >$ $[\mu m]$	$RMS_{\delta y}$ $[\mu m]$	a_z $[\mu m]$	b_z $[\mu m/m]$	$< \delta z >$ $[\mu m]$	$RMS_{\delta z}$ $[\mu m]$
HV-1	1.1 $\pm$2.4	2.1 $\pm$2.3	-14.3 $\pm$2.0	-4.4 $\pm$2.1	16.2 $\pm$1.1	-6.2 $\pm$4.9	-10.3 $\pm$2.5	-6.2 $\pm$4.9	19.3 $\pm$1.0
HV-2	-3.4 $\pm$1.4	3.9 $\pm$1.8	12.9 $\pm$1.8	1.6 $\pm$1.0	16.1 $\pm$1.0	-8.9 $\pm$5.0	4.6 $\pm$1.5	-8.9 $\pm$5.0	20.0 $\pm$0.9
HV-3	3.9 $\pm$3.3	-14.0 $\pm$3.0	-2.5 $\pm$2.3	2.8 $\pm$2.3	18.2 $\pm$1.9	16.2 $\pm$2.6	1.5 $\pm$1.9	16.2 $\pm$2.6	15.3 $\pm$1.4
HV-4	-10.4 $\pm$2.6	6.5 $\pm$3.9	17.4 $\pm$4.1	-3.8 $\pm$2.0	21.0 $\pm$0.8	-7.9 $\pm$4.7	0.0 $\pm$1.7	-7.9 $\pm$4.7	14.9 $\pm$0.8
HV-5	3.4 $\pm$1.4	3.1 $\pm$3.4	-9.7 $\pm$2.8	0.3 $\pm$1.2	14.1 $\pm$1.3	0.2 $\pm$3.7	-6.4 $\pm$2.8	0.2 $\pm$3.7	13.2 $\pm$0.7
HV-6	5.3 $\pm$2.3	1.8 $\pm$2.1	-5.7 $\pm$2.4	3.3 $\pm$1.9	24.7 $\pm$0.9	10.6 $\pm$3.4	-10.7 $\pm$1.6	10.6 $\pm$3.4	15.8 $\pm$0.6
RO-1	-2.4 $\pm$2.5	-3.6 $\pm$1.0	9.4 $\pm$1.3	1.3 $\pm$1.9	11.6 $\pm$0.2	-11.2 $\pm$5.5	-8.0 $\pm$1.3	-11.2 $\pm$5.1	11.9 $\pm$1.1
RO-2	3.5 $\pm$1.3	-2.3 $\pm$0.4	-11.8 $\pm$4.2	-1.1 $\pm$1.3	13.2 $\pm$0.6	4.7 $\pm$3.0	-8.3 $\pm$2.0	4.7 $\pm$3.0	11.4 $\pm$0.8
RO-3	-1.7 $\pm$2.1	3.3 $\pm$0.9	3.9 $\pm$2.1	-0.1 $\pm$1.7	17.6 $\pm$1.4	2.8 $\pm$2.0	-7.4 $\pm$2.8	2.8 $\pm$2.0	13.7 $\pm$1.7
RO-4	-2.9 $\pm$1.4	-10.8 $\pm$1.4	0.1 $\pm$0.3	-3.0 $\pm$1.5	14.7 $\pm$0.1	10.6 $\pm$3.5	5.8 $\pm$1.4	10.6 $\pm$3.5	15.2 $\pm$1.1
RO-5	12.4 $\pm$0.9	-4.6 $\pm$2.4	-13.0 $\pm$4.1	7.3 $\pm$0.8	18.7 $\pm$0.4	5.9 $\pm$3.9	-2.7 $\pm$1.4	5.9 $\pm$3.9	15.9 $\pm$0.9
RO-6	-8.4 $\pm$1.5	9.1 $\pm$1.5	10.9 $\pm$1.6	-4.4 $\pm$2.0	20.8 $\pm$1.4	-19.2 $\pm$4.3	1.9 $\pm$0.6	-19.2 $\pm$4.3	18.8 $\pm$0.7

7 Intermediate Scans

For chamber orientation r4, three successful scans have been performed at intermediate x-positions between the chamber ends (see Figure 1). The chamber parameters from the global fits to these data are given in Table 4. The RMS widths of the residual distributions for the top and bottom multilayer during the scans separately and combined are shown in Figures 10–12 and in Table 9 as function of x.

The wire positions measured at intermediate x-positions between the chambers ends (see Figure 1) show a smaller spread than at the HV and RO ends (see Table 9) because they are determined by interpolation between both ends and by the wire sag. Fluctuations in the wire sag of 2 μm RMS due to the variations of the measured wire tension within 1% RMS (see [2]) can be neglected. The expected widths of the residual distributions as function of x are therefore determined by

$$\sigma^{\rm res}_{y,z}(x) = \sqrt{\left(\frac{x}{L}\right)^2 \sigma^{\rm res\,2}_{y,z}(RO) + \left(\frac{x}{L}-1\right)^2 \sigma^{\rm res\,2}_{y,z}(HV)} \qquad (3)$$

where $L = 3800$ mm is the length of the tubes.

The results in Table 9 show that the measured values of $\sigma_{y,z}$ at intermediate x-positions are always larger than predicted from equation (3). A possible source of this discrepancy is the contribution of the X-ray measurement errors $\sigma^{\rm tomo}_{y,z}$ which do not interpolate. To account for this effect, the error propagation has to be modified:

$$\sigma^{\rm res}_{y,z}(x) = \sqrt{\left(\frac{x}{L}\right)^2 (\sigma^{\rm res\,2}_{y,z}(RO) - \sigma^{\rm tomo\,2}_{y,z}) + \left(\frac{x}{L}-1\right)^2 (\sigma^{\rm res\,2}_{y,z}(HV) - \sigma^{\rm tomo\,2}_{y,z})} \;\oplus\; \sigma^{\rm tomo}_{y,z}. \qquad (4)$$

The predictions for the X-ray tomograph measurement errors which describe the RMS values of the data with equation (4) are given in Table 9. These predictions are higher than the estimates from the reproducibility of repeated scans, especially for the z-coordinate.

Table 7: Measured z-pitch and z-shift (with respect to the fitted wire grid) for individual tube layers (average of all scans on HV and RO side, respectively). The layers are numbered in the sequence of glueing during chamber construction and from the inside out for each multilayer (multilayer 1: layers 1–3, multilayer 2: layers 4–5).

Layer no.	z-pitch [μm]		z-shift [μm]	
	HV side	RO side	HV side	RO side
1	30035.9 ± 0.08	30036.0 ± 0.04	$-\ 6 \pm 5$	$+11 \pm 6$
2	30036.3 ± 0.05	30036.0 ± 0.06	$-\ 9 \pm 5$	$-\ 5 \pm 3$
3	30036.3 ± 0.06	30036.0 ± 0.08	$+16 \pm 3$	$-\ 3 \pm 2$
4	30036.2 ± 0.05	30036.4 ± 0.04	$-\ 8 \pm 5$	-11 ± 4
5	30036.0 ± 0.08	30036.1 ± 0.04	0 ± 4	$-\ 6 \pm 4$
6	30035.9 ± 0.05	30036.3 ± 0.02	$+11 \pm 3$	$+19 \pm 4$
Average	30036.2 ± 0.1	30062.0 ± 0.05		

Table 8: Averaged measured y-distances [μm] between subsequent tube layers (numbering as in Table 7)

Layer no.	HV side	RO side	Design value
1–2	26064 ± 2.0	26058 ± 2	26046 ± 10
2–3	26059 ± 3.0	26061 ± 2	26061 ± 10
4–5	26054 ± 2.0	26050 ± 2	26041 ± 10
5–6	26055 ± 2.0	26072 ± 2	26066 ± 10
Average	26058 ± 0.5	26060 ± 1	26054 ± 10

Table 9: RMS widths of the residual distributions for 5 scans at different positions along the tubes in the same orientation r4 of the chamber (see Figure 1). The expectations according to equation (3) from interpolation of the wire locations between the fixed ends and the predicted X-ray tomograph resolutions $\sigma_{y,z}^{\text{tomo}}$ are also shown.

Scan	x-position [mm]	RMS_y^{tot} [μm] measured	RMS_z^{tot} [μm] measured	RMS_y^{tot} [μm] expected	RMS_z^{tot} [μm] expected
15	0 (HV side)	20.3	18.8	20.3	18.8
19	L/4	17.7	17.3	15.1	14.7
16	L/2 (Center)	15.0	16.1	12.9	13.5
18	3L/4	15.5	16.7	13.6	15.5
17	L (RO side)	17.0	19.7	17.0	19.7
				$\sigma_{y,\text{tot}}^{\text{tomo}} = 10.0$ μm	$\sigma_{z,\text{tot}}^{\text{tomo}} = 12.1$ μm
Scan	x-position [mm]	RMS_y^{top} [μm] measured	RMS_z^{top} [μm] measured	RMS_y^{top} [μm] expected	RMS_z^{top} [μm] expected
15	0 (HV side)	18.5	20.7	18.5	20.7
19	L/4	16.0	18.3	14.3	16.0
16	L/2 (Center)	12.6	13.8	11.8	13.0
18	3L/4	12.2	13.1	11.9	12.9
17	L (RO side)	14.6	15.7	14.6	15.7
				$\sigma_{y,\text{top}}^{\text{tomo}} = 6.3$ μm	$\sigma_{z,\text{top}}^{\text{tomo}} = 6.6$ μm
Scan	x-position [mm]	RMS_y^{bot} [μm] measured	RMS_z^{bot} [μm] measured	RMS_y^{bot} [μm] expected	RMS_z^{bot} [μm] expected
15	0 (HV side)	21.9	16.8	21.9	16.8
19	L/4	19.1	16.3	17.1	13.8
16	L/2 (Center)	16.9	17.9	14.5	14.1
18	3L/4	18.0	19.5	15.2	17.5
17	L (RO side)	18.9	22.7	18.9	22.7
				$\sigma_{y,\text{bot}}^{\text{tomo}} = 12.3$ μm	$\sigma_{z,\text{bot}}^{\text{tomo}} = 15.6$ μm

8 Comparison with X-ray Data for Individual Tubes

In Figures 13 and 14, the residuals (with respect to the fitted grid) of the y-coordinates of the wires from X-ray tomograph scans on the RO side are plotted against the y-displacements of the wires from the center of individual drift tubes measured with X-rays before chamber assembly (see [2]). Similar correlations exist for the z-coordinate.

The expected correlations between the two wire coordinate measurements are obvious, independent of the orientation of the chamber during the X-ray tomograph scans. Using a simple model with Gaussian errors, this information can be used to roughly disentangle and estimate the different contributions to the total uncertainty in the wire coordinates:

1. The positioning accuracy $\sigma^{\rm wire}$ of the wires inside individual drift tubes.
2. The resolution $\sigma^{\rm X-ray}$ of the X-ray measurements of individual drift tubes.
3. The positioning accuracy $\sigma^{\rm tube}$ of drift tubes in the chamber.
4. The average resolution $\sigma^{\rm tomo}$ of the X-ray tomograph measurements.

Since the four types of errors are statistically independent, they add quadratically to give the widths $\sigma^{\rm res}$, $\sigma^{\rm disp}$ and $\sigma^{\rm diff}$ of the distributions of the measured parameters shown in Figures 15 and 16, the residuals of the wire coordinates from the X-ray tomograph, the wire displacements measured in the individual drift tubes and the difference of the two correlated variables:

$$\sigma^{\rm res} = \sigma^{\rm wire} \oplus \sigma^{\rm tube} \oplus \sigma^{\rm tomo}, \tag{5}$$

$$\sigma^{\rm disp} = \sigma^{\rm wire} \oplus \sigma^{\rm X-ray}, \tag{6}$$

$$\sigma^{\rm diff} = \sigma^{\rm tube} \oplus \sigma^{\rm X-ray} \oplus \sigma^{\rm tomo}. \tag{7}$$

The average resolution $\sigma^{\rm tomo}$ of the X-ray tomograph over all chamber orientations has been estimated in section 4, equations (1) and (2). Therefore, the three equations (5)–(7) allow to determine the three unknown errors $\sigma^{\rm wire}$, $\sigma^{\rm tube}$ and $\sigma^{\rm X-ray}$. The standard deviations (from fit of a Gaussian) of the measured distributions, $\sigma^{\rm res}$ averaged over the scans, $\sigma^{\rm disp}$ and $\sigma^{\rm diff}$ (compare Figures 15 and 16 for two scans), and the values for $\sigma^{\rm wire}$, $\sigma^{\rm tube}$ and $\sigma^{\rm X-ray}$ calculated from them are given in Table 10 separately for the HV and RO side and the two multilayers numbered in the sequence of assembly.

The expection of larger z-positioning errors $\sigma_z^{\rm tube}$ on the HV side of multilayer 1 and on the RO side of multilayer 2 due to global z-shifts of the two outer tube layers (see section 6) is reproduced by the results.

Table 10: The uncertainties $\sigma^{\rm res}$, $\sigma^{\rm disp}$ and $\sigma^{\rm diff}$ in the wire coordinates measured by the X-ray tomograph (average of scans) and for indidvidual tubes and their difference and the errors $\sigma^{\rm wire}$, $\sigma^{\rm tube}$ and $\sigma^{\rm X-ray}$ determined from them separately for the two chamber ends and the two multilayers ML 1 and ML 2 numbered in the assembly sequence (all numbers in [μm]).

Side	Multilayer	Coord.	$\sigma^{\rm res}$	$\sigma^{\rm disp}$	$\sigma^{\rm diff}$	$\sigma^{\rm wire}$	$\sigma^{\rm tube}$	$\sigma^{\rm X-ray}$
HV	ML 1	y	16.6	14.4	16.3	10.4	11.4	10.0
HV	ML 2	y	12.8	10.4	10.9	8.8	7.1	5.5
RO	ML 1	y	17.2	12.6	15.0	10.7	12.0	6.7
RO	ML 2	y	16.0	11.6	11.9	11.2	9.8	3.2
HV	ML 1	z	17.6	8.6	16.5	7.5	15.5	4.2
HV	ML 2	z	12.5	11.1	11.0	8.9	8.0	6.6
RO	ML 1	z	10.5	9.2	9.8	7.0	7.0	6.0
RO	ML 2	z	15.3	11.5	16.0	7.4	12.9	8.8

9 Bad Wire Coordinates

Tails of the distributions of the residuals of the wire coordinates are caused by a few wire coordinates far away from the fitted grid. During drift tube testing and chamber assembly it was verified that such large deviations did not occur (see [2]). Therefore these wires most likely have been wrongly measured by the X-ray tomograph. They have, however, not been removed from the data sample for the grid fits. They are partly responsible for the rather large variations in the X-ray tomograph resolution for different chamber orientations (see section 4 and Table 3.

To estimate the effect of the "bad" wire coordinates on the RMS widths of the residual distributions, they have been fitted with a Gaussian and $\pm 3\sigma$- and $\pm 2\sigma$-cuts were applied which typically rejected 2% and 10% of the wires, respectively. The RMS values of the residual distributions after the cuts are shown in Table 11.

Table 11: RMS values and standard deviations σ (from fit of a Gaussian) of the residual distributions for the global fit to the X-ray tomograph measurements (average of all scans) before and after elimination of outlying wire coordinate measurements (in [μm]).

Side	RMS_y^{tot}	σ_y^{tot}	RMS_y^{tot} (3σ cut)	RMS_y^{tot} (2σ cut)
Average HV side	19.0 ± 0.8	17.6 ± 0.9	17.5 ± 0.8	15.4 ± 0.6
Average RO side	17.0 ± 0.2	14.8 ± 0.2	15.6 ± 0.2	13.0 ± 0.1
Side	RMS_z^{tot}	σ_z^{tot}	RMS_z^{tot} (3σ cut)	RMS_z^{tot} (2σ cut)
Average HV side	19.3 ± 0.8	17.3 ± 1.0	17.9 ± 0.6	15.1 ± 0.9
Average RO side	18.2 ± 1.3	15.9 ± 1.3	16.0 ± 1.2	13.9 ± 1.0

10 Conclusions

The complete X-ray tomograph data of the BOS prototype chamber have been analyzed. The results lead to the following conclusions:

1. From repeated scans of the chamber in the same position, the reproducibility and intrinsic accuracy of the X-ray tomograph measurements has been evaluated. On top of the systematic variations in the X-ray measurements of the geometrical chamber parameters (minimised by averaging over all scans), the average intrinsic resolution of the X-ray tomograph was estimated to be 6 μm rms for the y coordinate and 4 μm rms in z from the reproducibility of the measurements of the BOS prototype chamber.

2. The geometrical parameters of the prototype chamber are determined by fitting a wire grid to the measured wire coordinates with y- and z-pitch, multilayer (ML) separations in y and z and the global cross plate sag in the X-ray tomograph supports as free parameters.

After averaging over all scans, the chamber parameters and the RMS widths of the residual distributions for high voltage and readout side are the following (without cut against outlying wire coordinate measurements):

	HV side		RO side	
	X-ray	Design value	X-ray	Design value
y-pitch [μm]	26058 ± 0.5	26054 ± 10	26060 ± 1.3	26054 ± 10
z-pitch [μm]	30036.2 ± 0.1	30036.8 ± 0.6	30036.2 ± 0.05	30036.8 ± 0.6
y sep. ML [mm]	347.041 ± 0.011	347.040 ± 0.010	347.078 ± 0.012	347.072 ± 0.010
z-sep. ML [μm]	-8 ± 11	0 ± 10	3 ± 16	0 ± 10
Including X-ray tomograph resolution:				
RMS$_y$ [μm]	19.0 ± 0.8		17.0 ± 0.2	
RMS$_z$ [μm]	19.3 ± 0.8		18.2 ± 1.3	
Wire locations with X-ray tomograph resolution subtracted:				
RMS$_y$ [μm]	18.0 ± 0.8		15.9 ± 0.2	
RMS$_z$ [μm]	19.0 ± 0.8		17.8 ± 1.3	

The fitted parameters are in good agreement with the design values (at 20°C); uncertainties in the wire locations are below the required 20 μm rms.

The design parameters of the prototype chamber (at 20°C) determined by the assembly jigging are well reproduced by the X-ray tomograph data within the measurement errors. The wires have been positioned in the whole chamber with an accuracy which is better than the required 20 μm RMS.

3. A further important achievement for the validation of the chamber assembly procedure is the good uniformity of the z-pitch and of the y-separation of all tube layers.

   The only significant deviations from the design parameters of the chamber are global shifts in z of the two outer tube layers by $+16$ μm and -19 μm, respectively, with respect to the fitted grid, layer 3 in the assembly sequence on the high-voltage side and layer 6 on the readout side. The two shifts of equal size and same direction in the coordinate frame of the assembly jigging can be attributed to the same sphere tower interface being outside tolerances in the z-displacement of $\pm 10\mu$m. Because of the z-shifts, the RMS width for the z-coordinate is larger than for y in spite of the uniform z-pitch.

4. Both with the cross plate sag monitors and from the X-ray tomograph data, global gravitational sags of the high voltage and readout ends of the prototype chamber were found which are larger than expected from the Bessel support of the cross plates and which vary from scan to scan. Obviously the chamber was not supported free of external moments in the tomograph. Kinematical mounts as in ATLAS should be used to support the chambers for the X-ray tomograph measurements.

   To evaluate the accuracy of the chamber construction, it is necessary to take the global deformation into account by fitting a common parabola for all layers. Beyond this global correction, no systematic deformations of individual tube layers were found.

Acknowledgments

The authors gratefully acknowledge Hermann Wellenstein for helpful discussions.

References

[1] D. Drakulakos et al., *The High-Precision X-ray Tomograph for Quality Control of the ATLAS MDT Muon Spectrometer*, CERN-OPEN-97-023, July 1997.

[2] V.Bartheld et al., *Construction of the Full-Scale Prototype of a BOS MDT Chamber*, ATL-MUON-98-256, October 1998.

[3] *ATLAS Muon Spectrometer–Technical Design Report*, CERN/LHCC/97-22, ATLAS TDR 10, 31 May 1997.

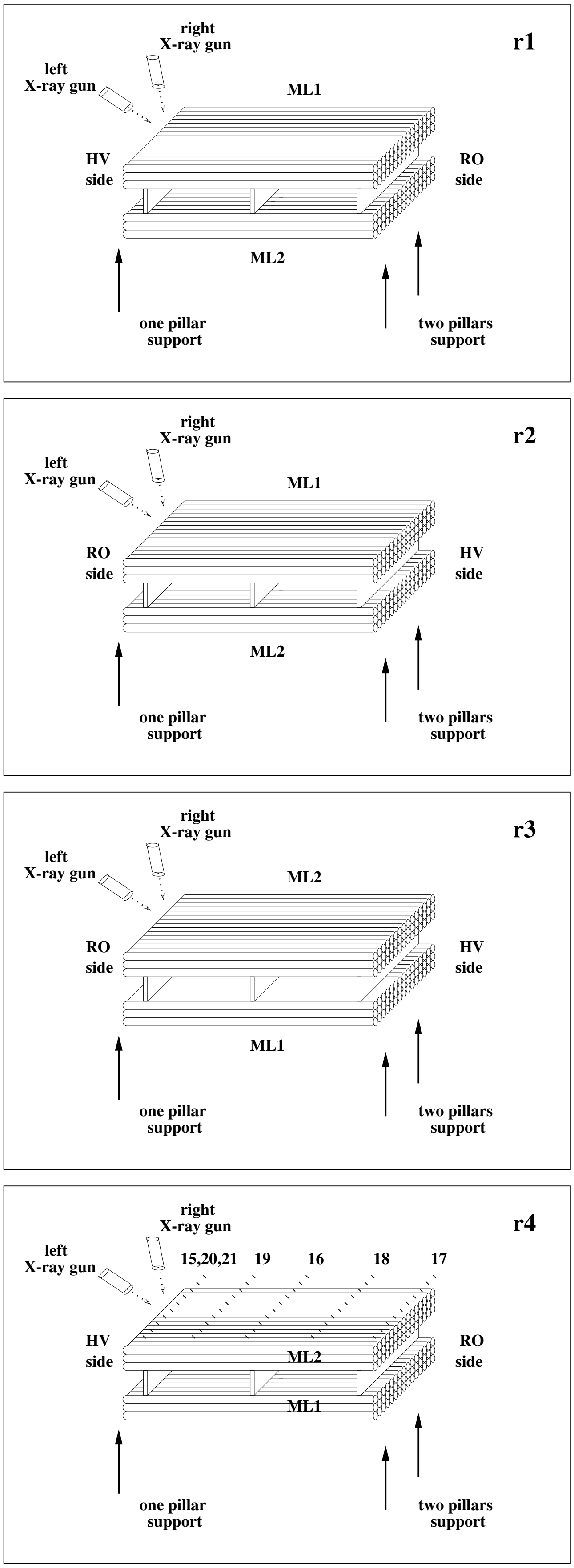

Orientation r1

HV scans: 07, 08

RO scans: NONE

Orientation r2

HV scans: 09, 11

RO scan: 10

Orientation r3

HV scans: 12, 14

RO scan: 13

Orientation r4

HV scans: 15, 20, 21

RO scan: 17

Interm. scans: 16, 18, 19

Fig. 1: The orientations of the prototype chamber (r1, r2, r3, r4) during the X-ray tomograph measurements. The two multilayers ML1 and ML2 are numbered in the assembly sequence.

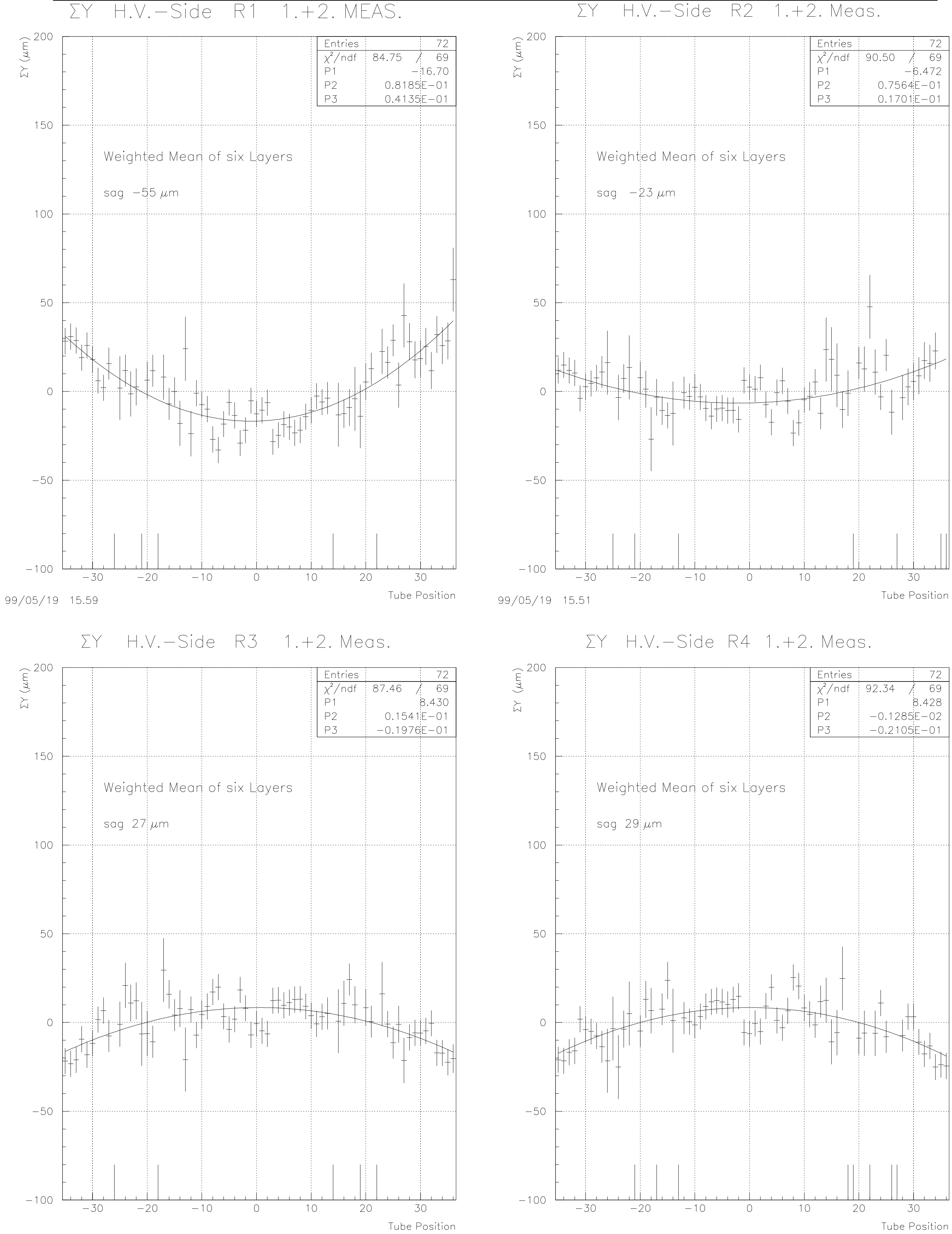

Fig. 2: Average of the y-residuals of the wires in the six tube layers as a function of the z-coordinate for the 4 orientations (r1, r2, r3, r4) of the HV-side of the chamber.

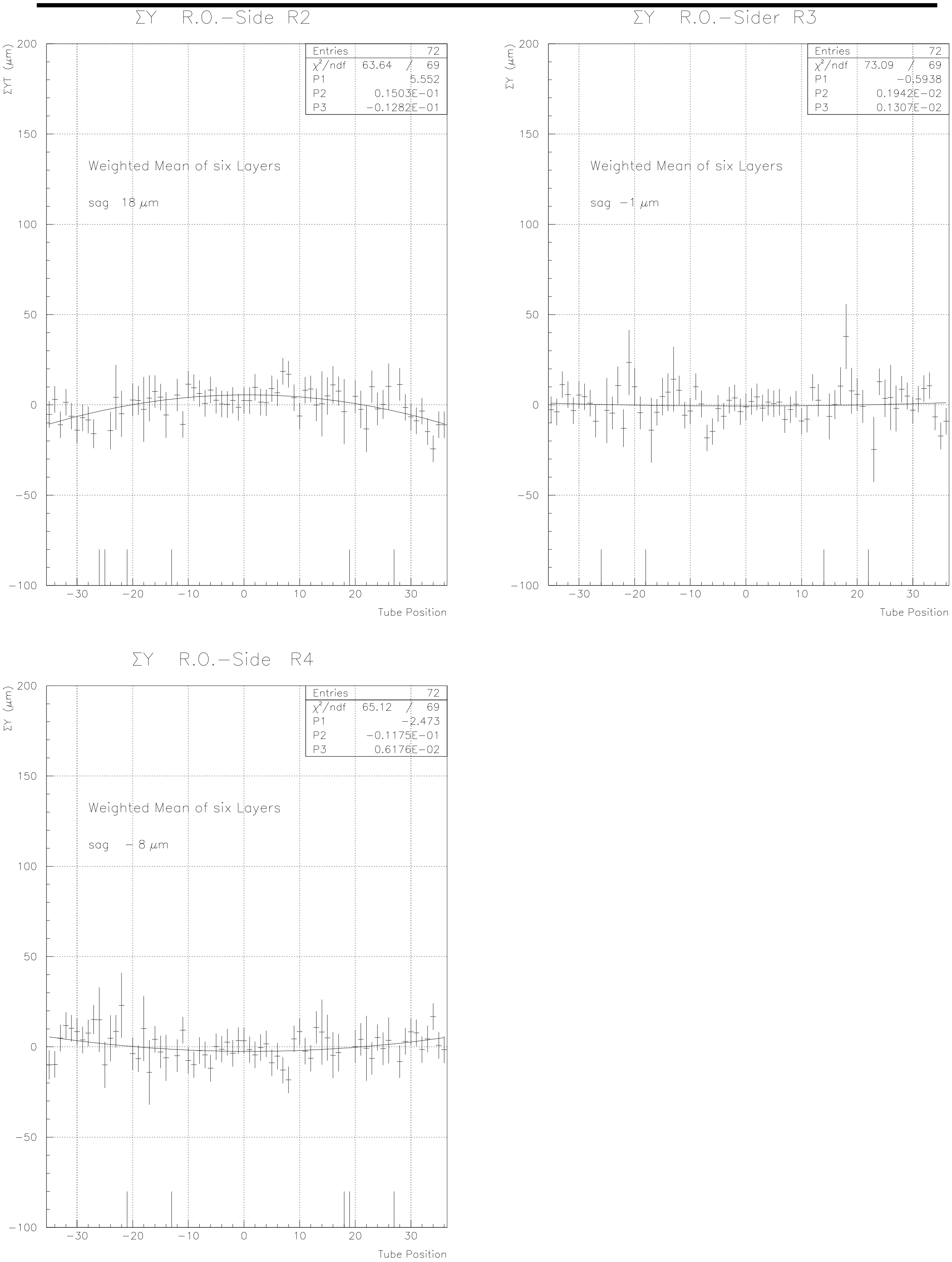

Fig. 3: Average of the y-residuals of the wires in the six tube layers as a function of the z-coordinate for the three orientations (r2, r3, r4) of the RO-side of the chamber.

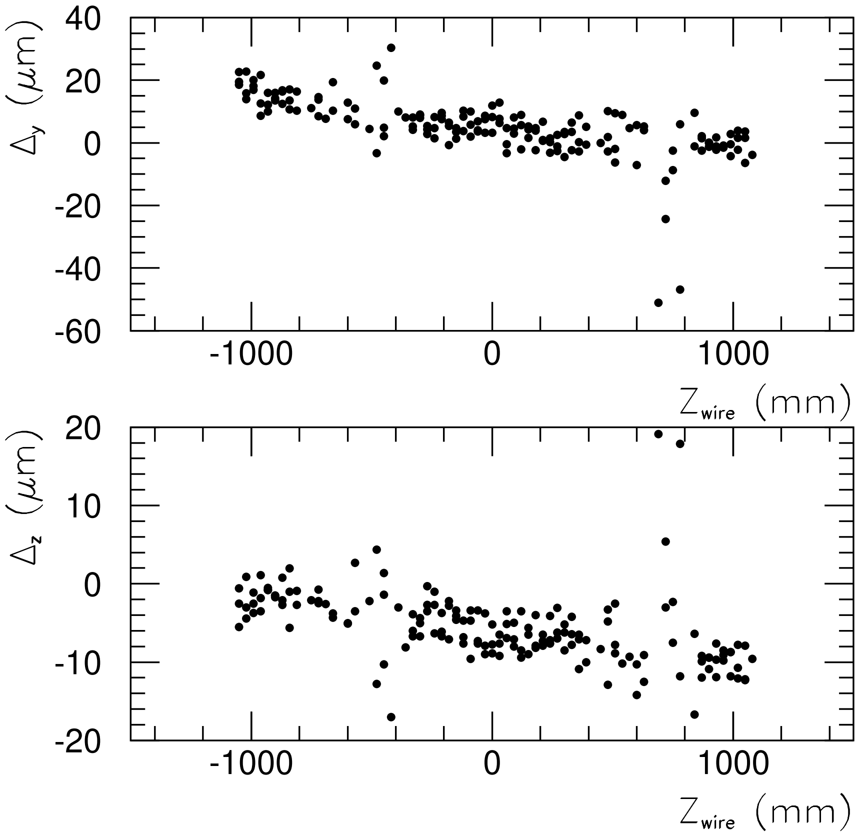

Fig. 4: Differences of the residuals of the measured wire positions in y and z in the top multilayer for scans no. 7 and 8 as functions of the wire position in z.

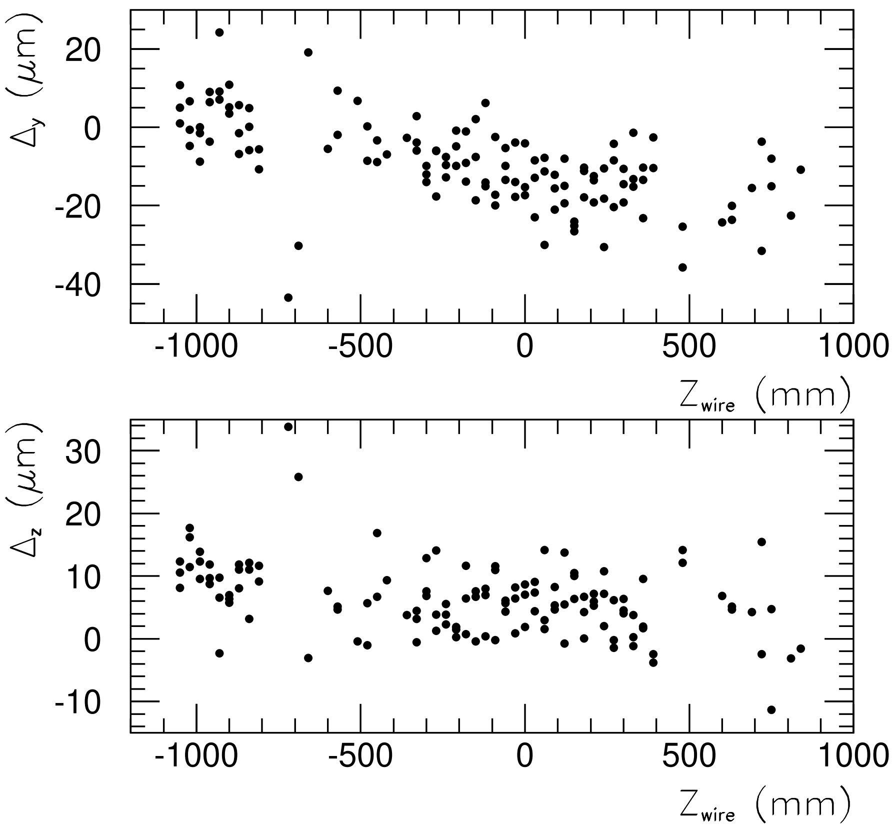

Fig. 5: Differences of the residuals of the measured wire positions in y and z in the bottom multilayer for scans no. 7 and 8 as functions of the wire position in z.

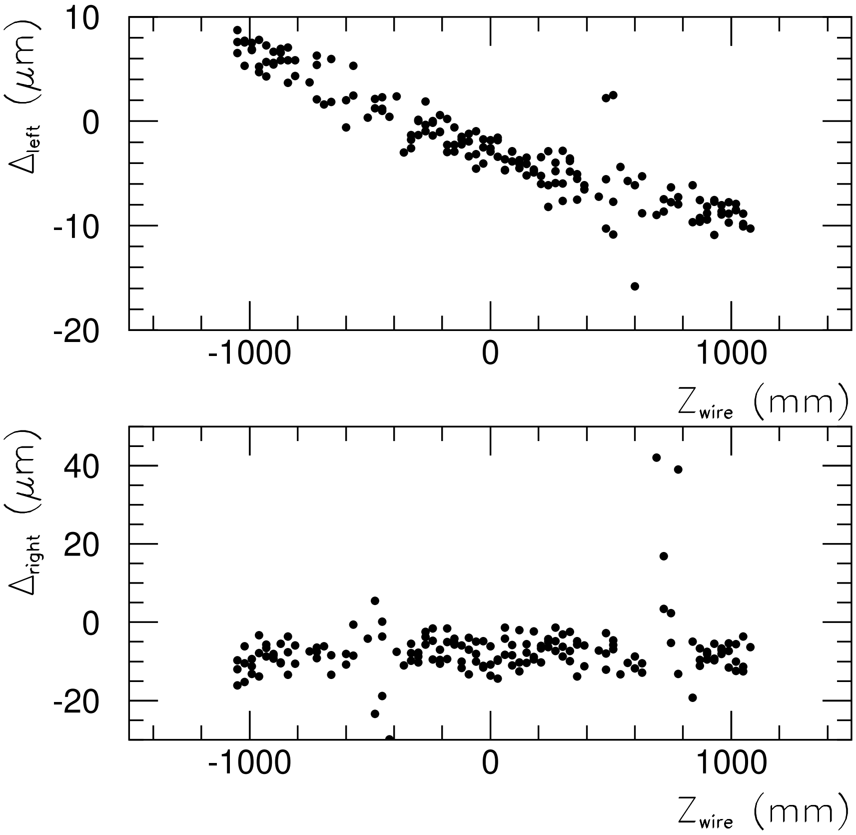

Fig. 6: Differences of the residuals of the projected wire coordinates measured with the left and the right X-ray beam in the top multilayer for scans no. 7 and 8 as functions of the wire position in z.

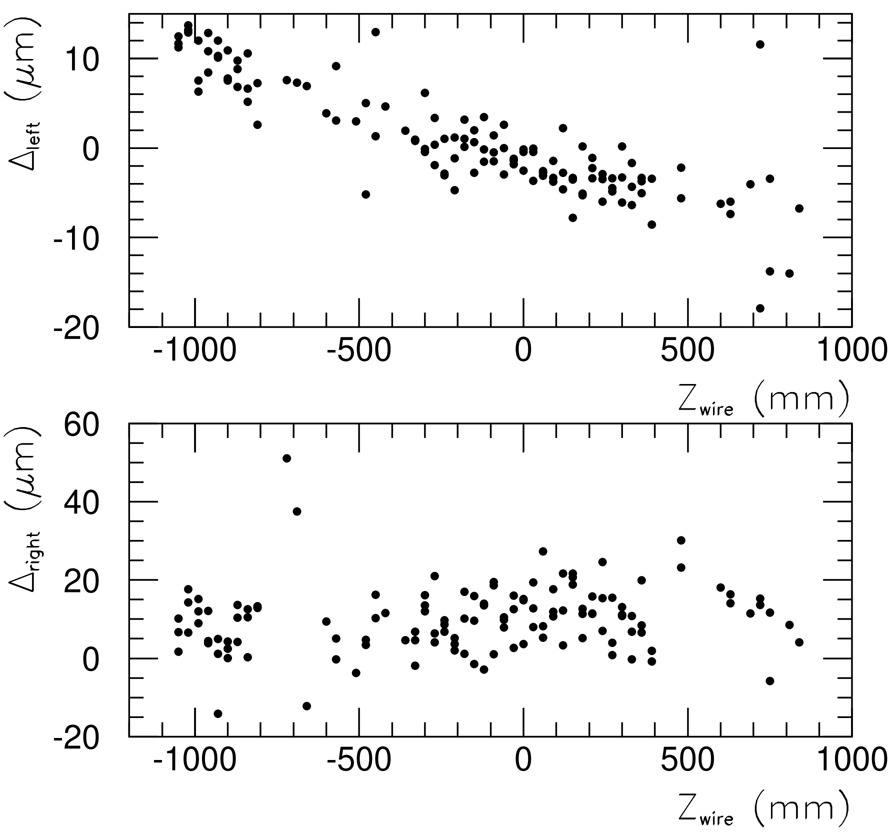

Fig. 7: Differences of the residuals of the projected wire coordinates measured with the left and the right X-ray beam in the bottom multilayer for scans no. 7 and 8 as functions of the wire position in z.

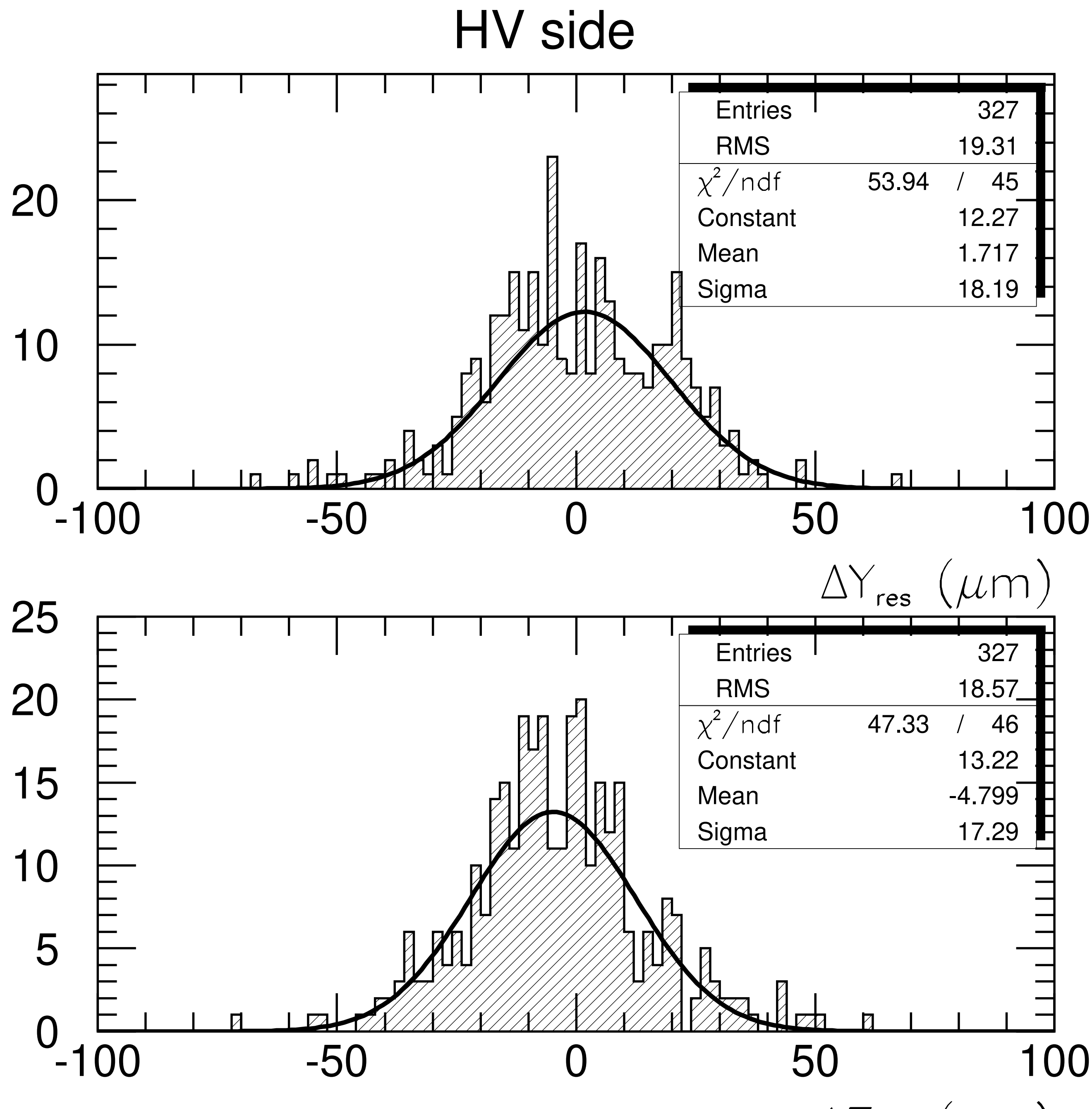

Fig. 8: Distributions of the residuals of the wire positions measured by the X-ray tomograph on the high voltage (HV) side (scan no. 20) with respect to the fitted wire grid.

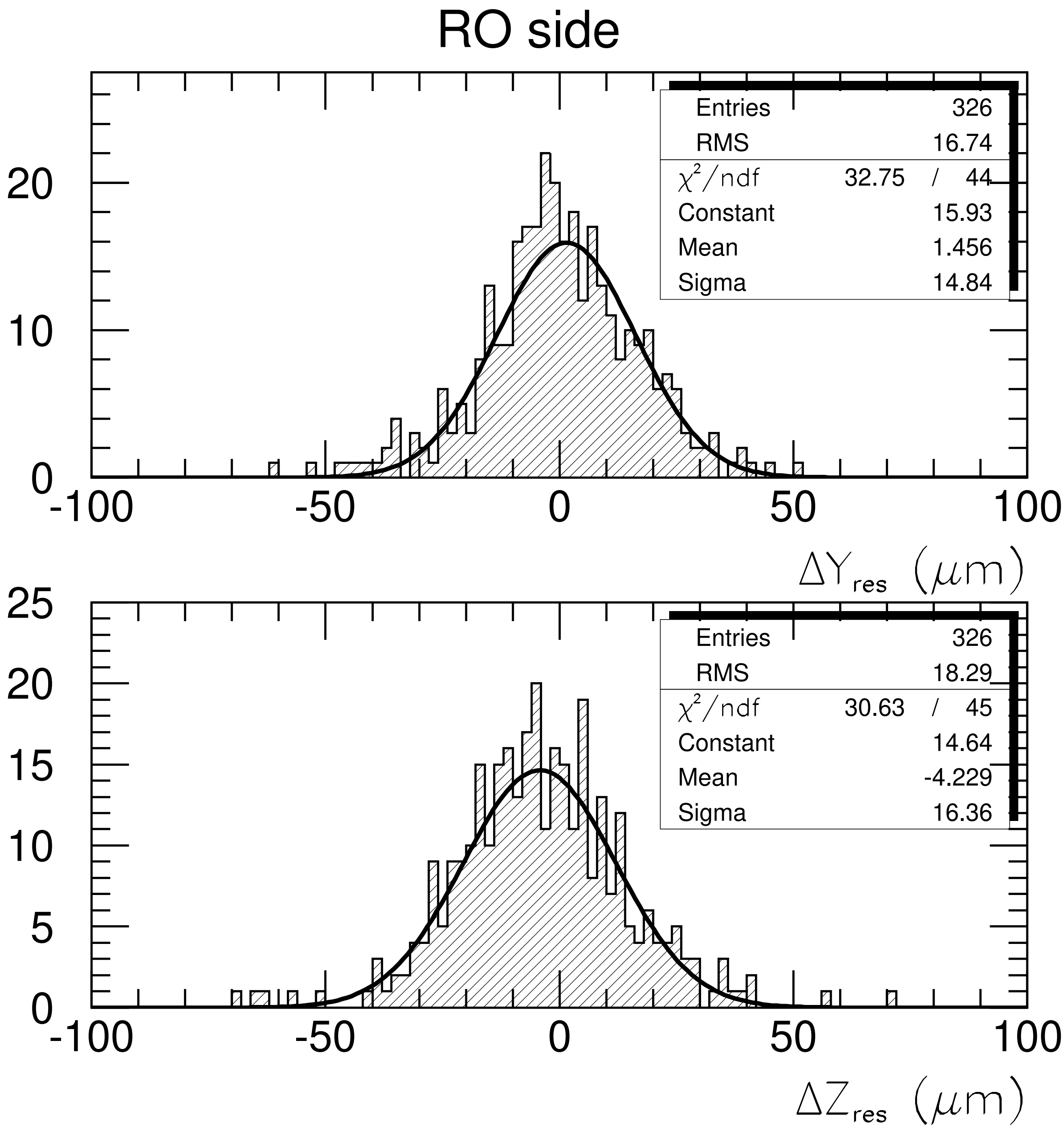

Fig. 9: Distributions of the residuals of the wire positions measured by the X-ray tomograph on the high voltage (RO) side (scan no. 13) with respect to the fitted wire grid.

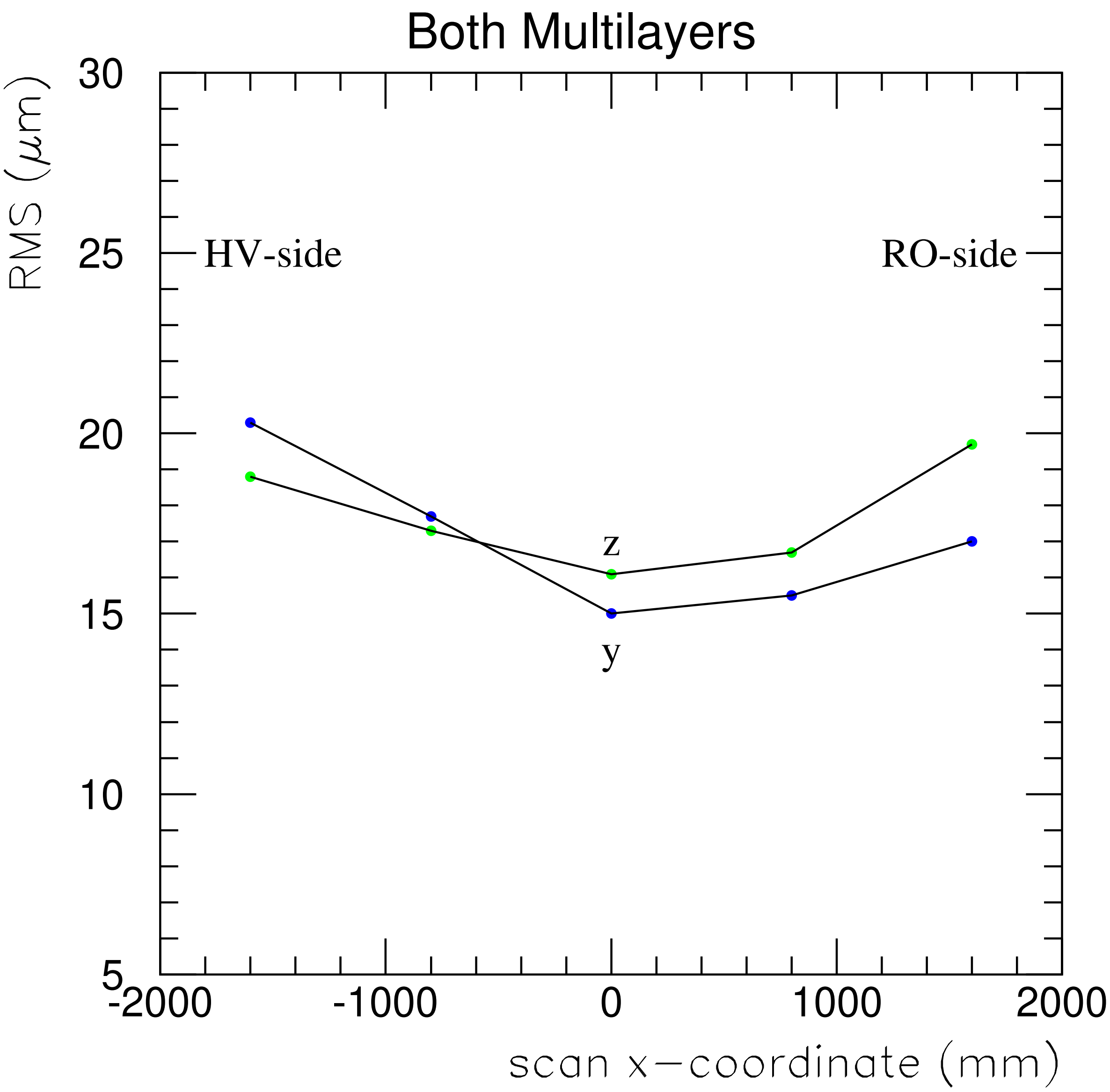

Fig. 10: The widths $RMS_y and RMS_z$ of the residual distributions of the global fit to the wire coordinates of both multilayers for scans no. 20, 19, 16, 18 and 17 at increasing x from the HV to the RO side of the chamber in the same orientation r4.

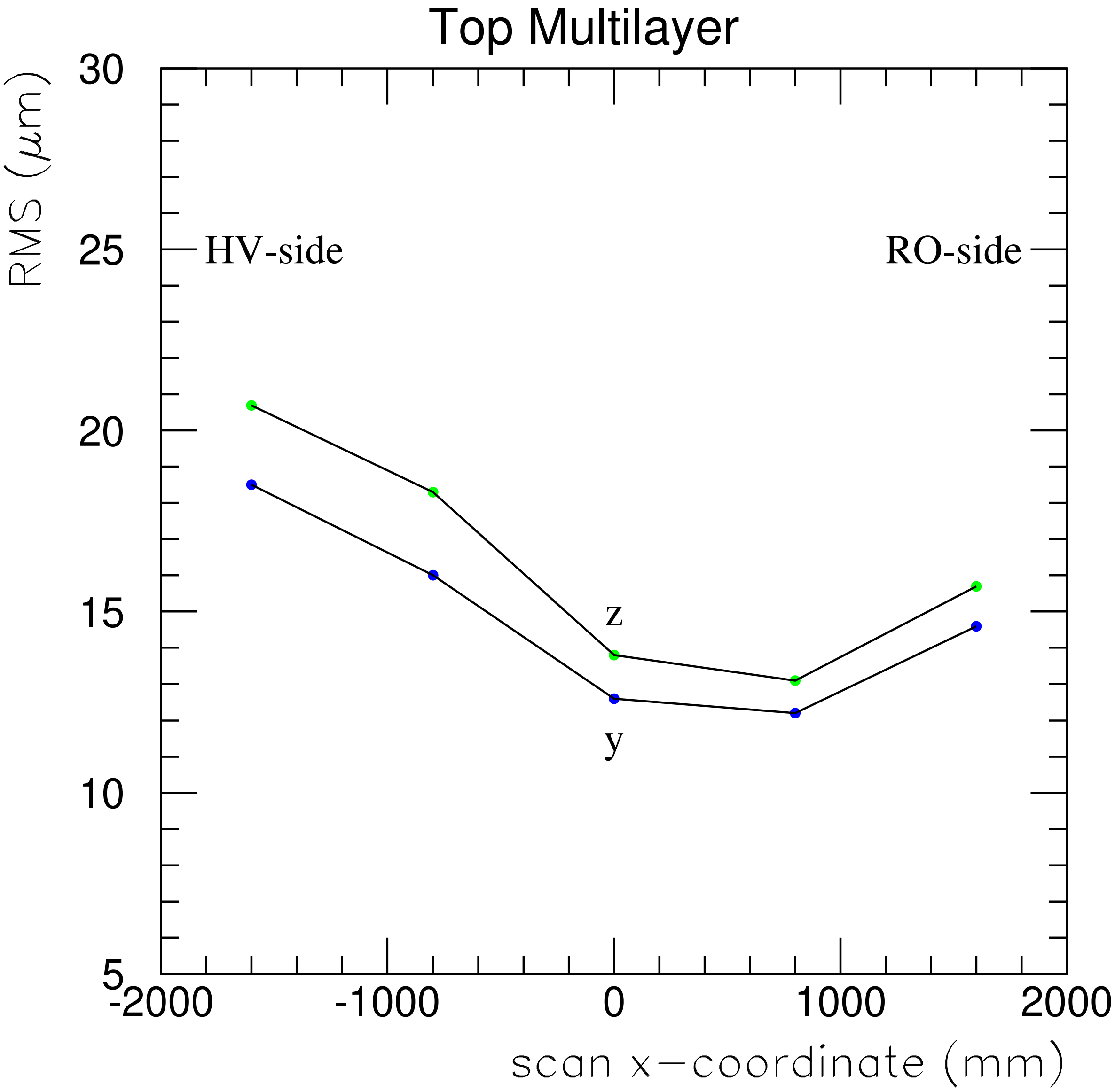

Fig. 11: The widths RMS_y and RMS_z of the residual distributions of the global fit to the wire coordinates of the top multilayer for scans no. 15, 19, 16, 18 and 17 at increasing x from the HV to the RO side of the chamber in the same orientation r4.

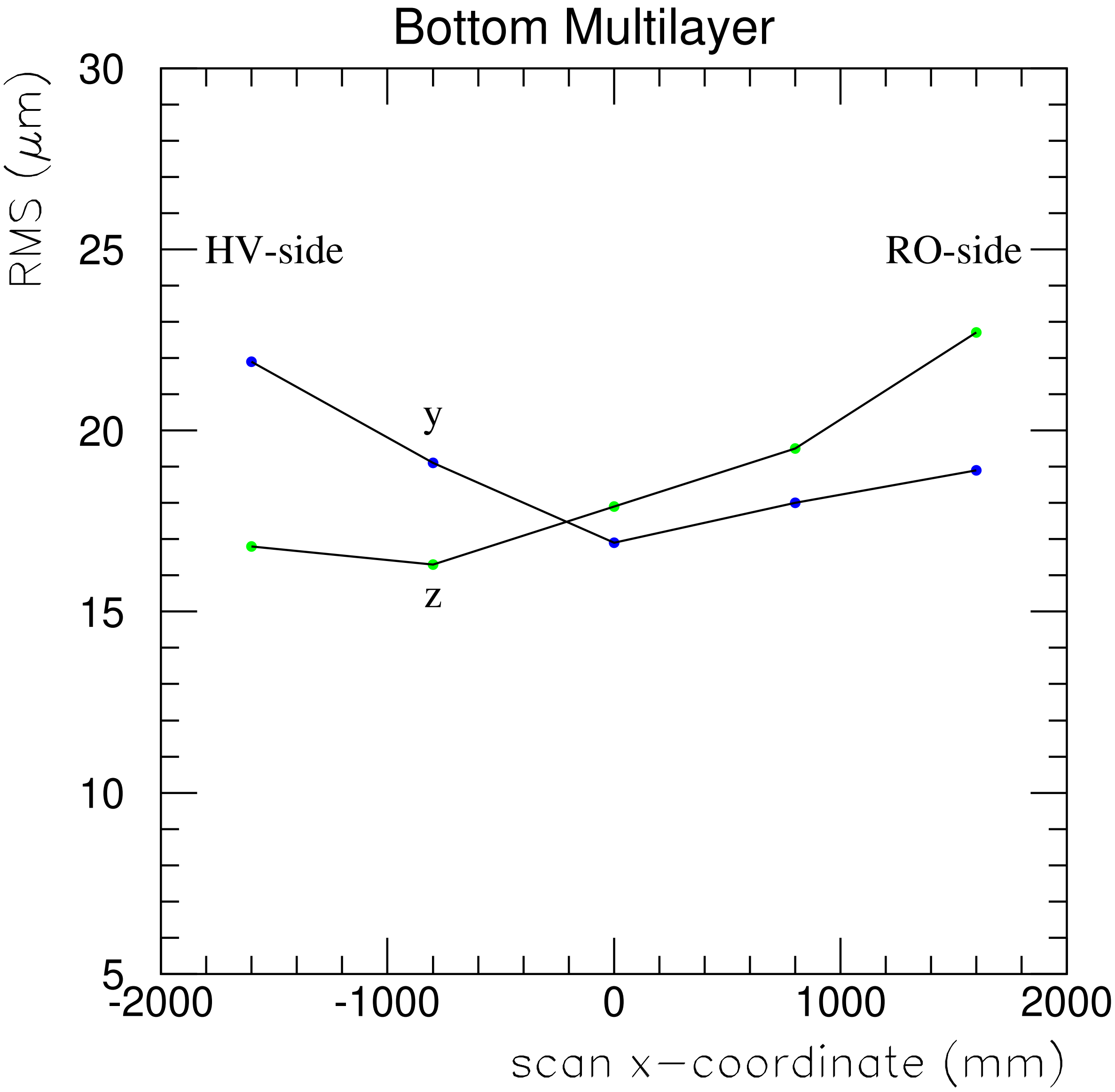

Fig. 12: The widths RMS_y and RMS_z of the residual distributions of the global fit to the wire coordinates of the bottom multilayer for scans no. 15, 19, 16, 18 and 17 at increasing x from the HV to the RO side of the chamber in the same orientation r4.

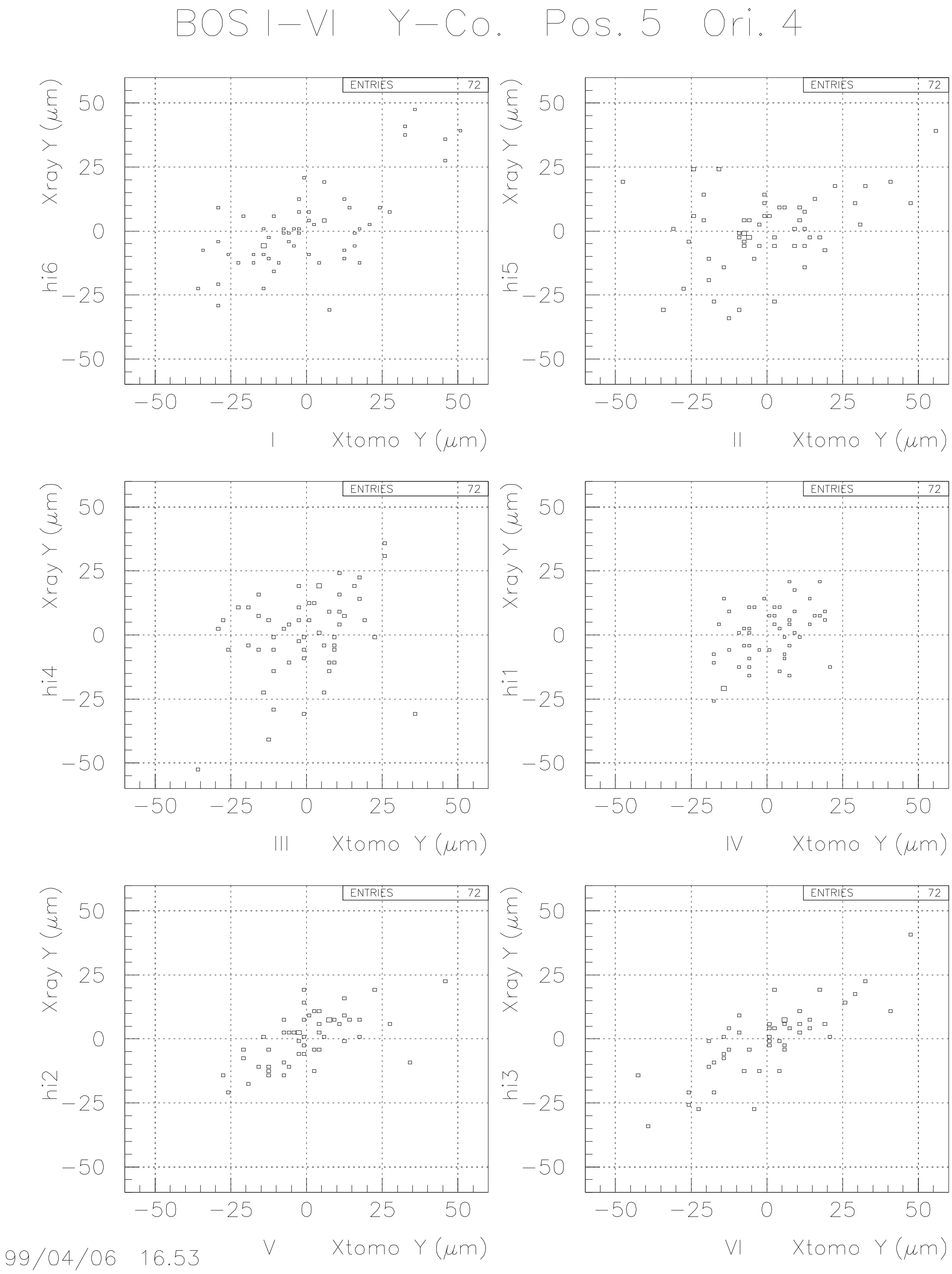

Fig. 13: Correlations of the residuals of the y-coordinates measured by the X-ray tomograph (Xtomo) with the y-displacements of the wires from the center measured in individual drift tubes with X-rays before assembly (Xray) (for the 6 tube layers on the RO side in orientation r4 of the chamber).

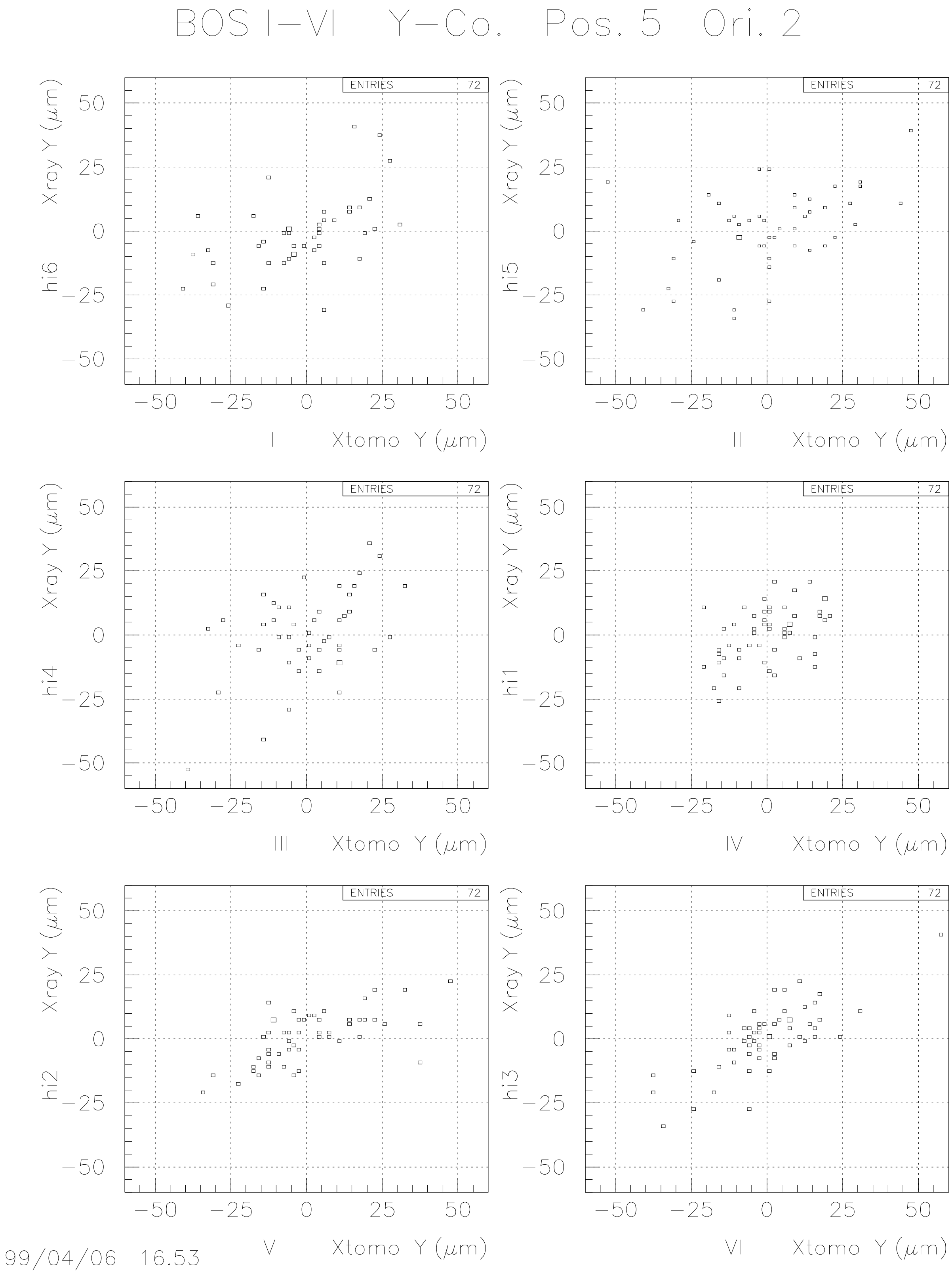

Fig. 14: Correlations of the residuals of the y-coordinates measured by the X-ray tomograph (Xtomo) with the y-displacements of the wires from the center measured in individual drift tubes with X-rays before assembly (Xray) (for the 6 tube layers on the RO side in orientation r2 of the chamber).

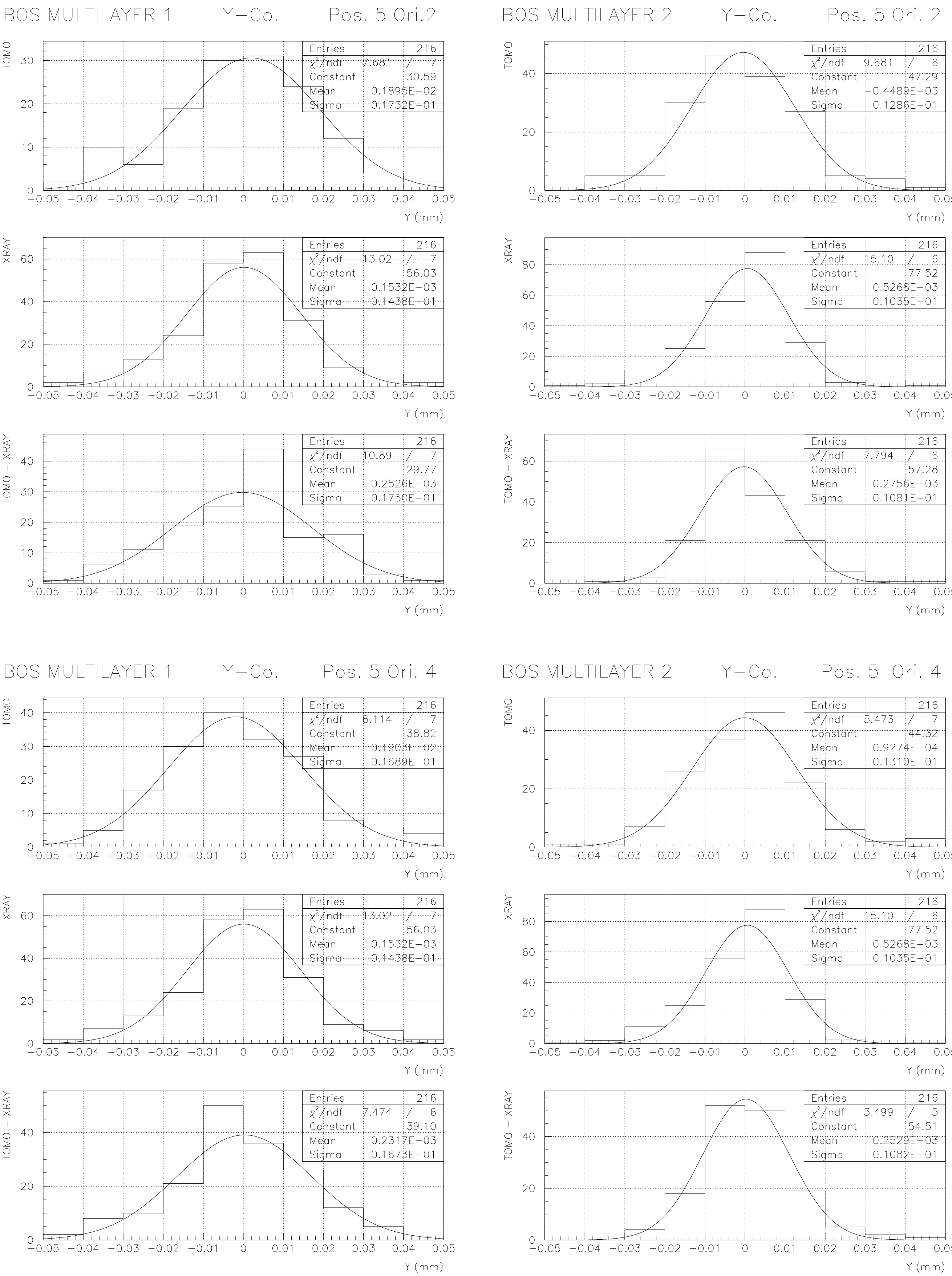

Fig. 15: Distributions of the residuals of the y-coordinates of the wires from the X-ray tomograph (TOMO), of the y-displacements of the wires measured in individual tubes (XRAY) and of their difference for the RO side and separately for the two multilayers (ML1: layers 1–3, ML2: layers 4–6) in the orientations r2 and r4 of the chamber.

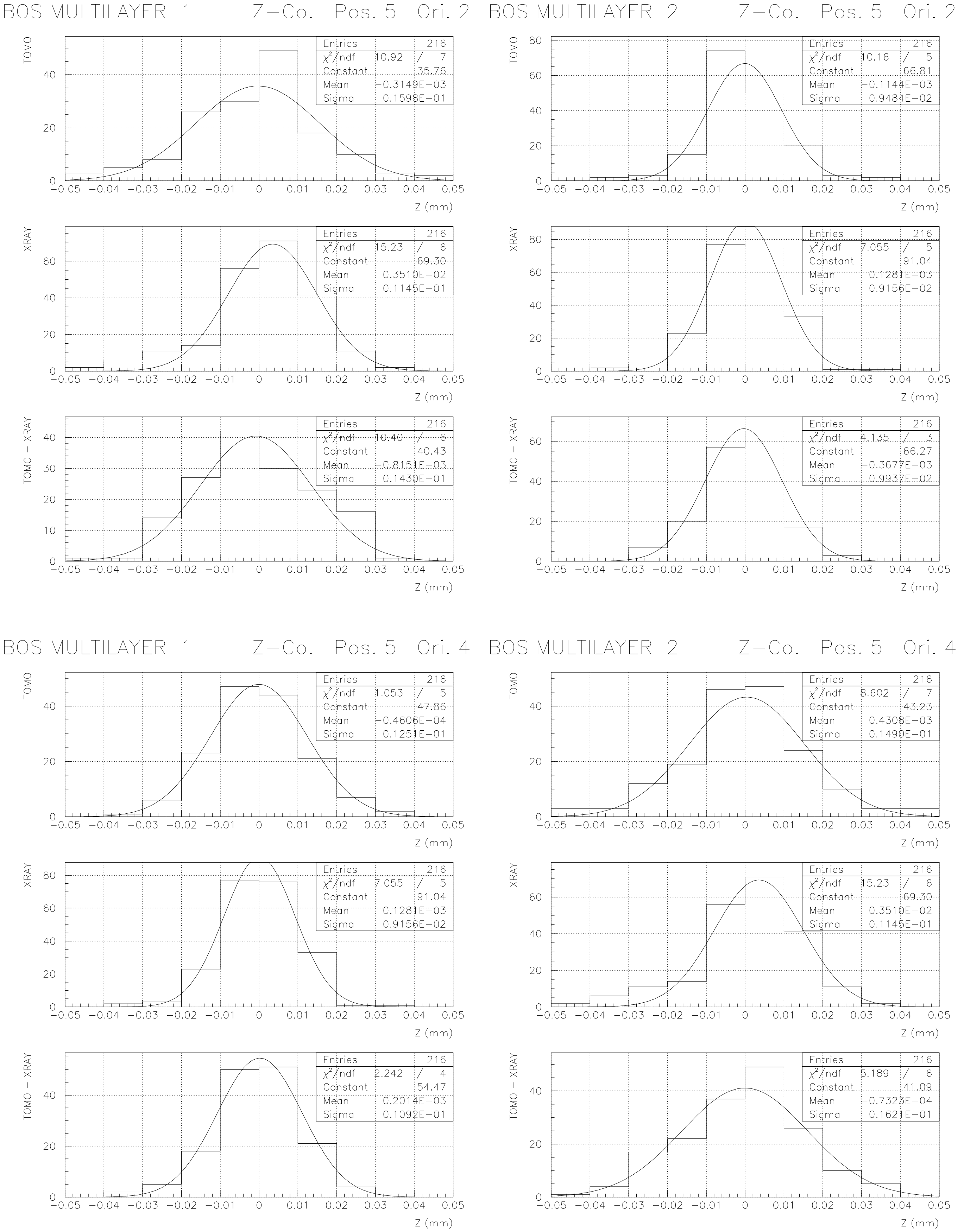

Fig. 16: Distributions of the residuals of the z-coordinates of the wires from the X-ray tomograph (TOMO), of the z-displacements of the wires measured in individual tubes (XRAY) and of their difference for the RO side and separately for the two multilayers (ML1: layers 1–3, ML2: layers 4–6) in the orientations r2 and r4 of the chamber.